JGR Space Physics

RESEARCH ARTICLE
10.1029/2019JA027541

Special Section:
Cluster 20th Anniversary: Results from the First 3D Mission

# Convection in the Magnetosphere-Ionosphere System: A Multimission Survey of Its Response to IMF $B_y$ Reversals

**N. A. Case[1], A. Grocott[1], R. C. Fear[2], S. Haaland[3,4], and J. H. Lane[1]**

[1]Department of Physics, Lancaster University, Lancaster, UK, [2]School of Physics and Astronomy, University of Southampton, Southampton, UK, [3]Max Planck Institute for Solar System Research, Göttingen, Germany, [4]Birkeland Centre for Space Science, University of Bergen, Bergen, Norway

**Abstract** Past studies have demonstrated that the interplanetary magnetic field (IMF) $B_y$ component introduces asymmetries in the magnetosphere-ionosphere (M-I) system, though the exact timings involved are still unclear with two distinct mechanisms proposed. In this study, we statistically analyze convective flows from three regions of the M-I system: the magnetospheric lobes, the plasma sheet, and the ionosphere. We perform superposed epoch analyses on the convective flows in response to reversals in the IMF $B_y$ orientation, to determine the flow response timescales of these regions. We find that the lobes respond quickly and reconfigure to the new IMF $B_y$ state within 30–40 min. The plasma sheet flows, however, do not show a clear response to the IMF $B_y$ reversal, at least within 4 hr postreversal. The ionospheric data, measured by the Super Dual Auroral Radar Network (SuperDARN), match their counterpart magnetospheric flows, with clear and prompt responses at ≥75° magnetic latitude (MLAT) but a less pronounced response at 60–70 MLAT. We discuss the potential implication of these results on the mechanisms for introducing the IMF $B_y$ component into the M-I system.

**Key Points:**
- Flows in the magnetotail lobes respond promptly to changes in the IMF $B_y$ orientation, reaching a new state within 30–40 min
- No clear flow response is detected on timescales of up to 4 hr in the plasma sheet
- Ionospheric flows exhibit clear responses at higher latitudes and a less pronounced responses at lower latitudes

**Correspondence to:**
N. A. Case,
n.case@lancaster.ac.uk

**Citation:**
Case, N. A., Grocott, A., Fear, R. C., Haaland, S., & Lane, J. H. (2020). Convection in the magnetosphere-ionosphere system: A multimission survey of its response to IMF $B_y$ reversals. *Journal of Geophysical Research: Space Physics*, *125*, e2019JA027541. https://doi.org/10.1029/2019JA027541

Received 15 OCT 2019
Accepted 16 SEP 2020
Accepted article online 2 OCT 2020



## 1. Introduction

The Earth's magnetosphere and ionosphere are intrinsically coupled, with the processes and dynamics in one linked to the processes and dynamics of the other via electric fields, magnetic field-aligned currents, and particle exchange (Blanc, 1988). This magnetosphere-ionosphere (M-I) system is also coupled with the external driving of the solar wind and the embedded interplanetary magnetic field (IMF). Changes in the upstream driving, for example, in the solar wind dynamic pressure or the orientation of the IMF, induce changes into the M-I system as a whole.

Past studies have clearly demonstrated that the orientation of the east-west component of the IMF, more commonly referred to as the IMF $B_y$ component, controls many different aspects of the M-I system. For example, a nonzero IMF $B_y$ component shifts the site of dayside reconnection (Park et al., 2006), introduces twisting of the magnetotail (e.g., Cowley, 1981; Russell, 1972), and produces directionally dependent fast flows in the magnetotail associated with untwisting (Grocott et al., 2007; Pitkänen et al., 2013). In the ionosphere, the IMF $B_y$ component drives asymmetries in the aurora (e.g., Østgaard et al., 2004; Reistad et al., 2013), including in transpolar arcs (e.g., Fear & Milan, 2012), and forms large-scale morphological changes to the ionospheric convection patterns (e.g., Grocott, 2017; Ruohoniemi & Greenwald, 2005).

Large-scale convection in the Earth's magnetosphere is primarily driven by dayside reconnection as described by the Dungey cycle (Dungey, 1961). Under southward IMF conditions, newly opened field lines transfer from the dayside magnetopause, across the polar cap, and into the nightside magnetotail. Once in the magnetotail, the field lines are forced down to the neutral sheet region, where they reconnect with oppositely directed field lines from the opposite lobe and propagate earthward. Due to the pileup in the nightside near-Earth region, the field lines then convect around the Earth back to the dayside, where the cycle repeats. In the magnetotail, convective flows are primarily in the duskward direction in the premidnight sector and dawnward in the postmidnight sector (e.g., Hori et al., 2000; Kissinger et al., 2012).

Under nonzero IMF $B_y$ conditions, certain asymmetries in the M-I system's convective flows develop. At the dayside magnetopause, the region of maximum shear and reconnection is shifted northward in the dusk

sector and southward in the dawn sector for positive IMF $B_y$. For negative $B_y$ the shift is reversed. In the lobes, this asymmetric flux loading results in a net flow across the noon-midnight meridian whose direction is dependent upon the orientation of the IMF $B_y$ component (Case et al., 2018; Cowley, 1981; Haaland et al., 2008). In the Northern Hemisphere (NH), under IMF $B_y > 0$ conditions, flows are predominantly in the $+Y$ direction, and in the Southern Hemisphere (SH) are predominantly in the $-Y$ direction. When the IMF $B_y$ orientation is reversed, so too are the predominate flow directions (Case et al., 2018; Haaland et al., 2008). Since the ionosphere and magnetosphere are intrinsically linked, asymmetries in the ionospheric convection are also created when there is an IMF $B_y$ component present. Large-scale differences in the ionospheric potentials are observed, creating different flow patterns (consisting of a number of distinct "cells") whose morphologies and size are dependent upon the IMF $B_y$ orientation (e.g., Cowley & Lockwood, 1992; Ruohoniemi & Greenwald, 2005) and hemisphere (e.g., Pettigrew et al., 2010). In particular, the antisunward flow across the polar cap is deflected by the IMF $B_y$ component, resulting in the $Y$ component of the flow switching orientation in response an IMF $B_y$ reversal (Haaland et al., 2007).

In the plasma sheet too, the average convective flow develops an interhemispheric asymmetry under nonzero IMF $B_y$ conditions, with the flows being preferentially directed in opposite directions in the two hemispheres based on the orientation of the IMF $B_y$ component (Pitkänen et al., 2019).

The $B_y$ component of the IMF which is imparted on the dayside field lines is transferred into the nightside too, though the timescales and mechanisms for this remain unclear (e.g., Case et al., 2018). For example, studies by Fear and Milan (2012) and Browett et al. (2017) have shown that the effect of the IMF $B_y$ component is introduced into the tail on timescales that match the traditional Dungey-cycle-driven picture (e.g., 2–4 hr) presented by Cowley (1981) and Cowley and Lockwood (1992) (hereafter referred to as the "Cowley explanation"). However, recent work has also shown that the $B_y$ component could be introduced on much shorter timescales through pressure forces on the inner magnetotail (e.g., Khurana et al., 1996; Tenfjord et al., 2015, 2017) (hereafter referred to as the "Tenfjord explanation"). The result of both of these methods, however, is the same: a twisting of the magnetotail (e.g., Cowley, 1981; Russell, 1972) which, in turn, creates an asymmetry in the flow direction as field lines convect back around to the dayside (e.g., Grocott et al., 2007).

When attributing phenomena or the responses of certain regions to a particular IMF $B_y$ state, previous studies have used a range of times over which to average the IMF $B_y$ component. For example, Pitkänen et al. (2013, 2017) used a 130 min average of the IMF $B_y$ preceding their "fast flow" events in the plasma sheet for characterization of these events. Others have used, or have suggested, timescales ranging from 45 min to over 3 hr for the IMF $B_y$ component to propagate into the tail (e.g., Browett et al., 2017; Fear & Milan, 2012; Pitkänen et al., 2016). The Tenfjord explanation, however, in which information is thought to be propagated by pressure waves rather than "penetration," is proposed to operate with timescales of the order of 15 min.

Additionally, there is some ambiguity around what is defined as a response. There is both a *response time*, in which the magnetosphere or ionosphere starts to change based on the new IMF $B_y$ orientation (which itself has to be time lagged from the bow shock to the magnetopause), and then a *reconfiguration time*, in which the magnetosphere or ionosphere has reached its "end state" based on this new orientation. Some studies have attempted to address this, for example, Grocott and Milan (2014) and Tenfjord et al. (2017). Grocott and Milan (2014), for example, showed that the ionosphere could respond quickly to changes in the IMF but took much longer to fully reconfigure. Other studies, such as modeling work by Kabin et al. (2003), however, showed much shorter reconfiguration times (15–20 min).

Determining a response time is further complicated by the possibility that the response time of a particular magnetotail phenomenon may occur on a different timescale to that of simply introducing the IMF $B_y$ component into the magnetotail. For example, as discussed in Cowley (1981), the convection of the IMF field lines with a $B_y$ into the magnetotail produces a nonuniform distribution (in the $Y$-$Z$ plane) of open field lines crossing the magnetopause. This results in a torque which, in turn, twists the magnetotail. One can envisage that the twisting of the magnetotail may take far less time to develop than the time required for the effects of the IMF $B_y$ component to be fully introduced into the tail, if only a small amount of torque is required to develop this twist. In such a scenario, the required torque may be sufficiently provided by the newly introduced $B_y$ component in the lobes well before the $B_y$ component has fully developed in the tail. Alternatively, the tail twisting time may be longer than the time required for the $B_y$ component to be introduced if a large amount of torque were to be required—whether this be to simply develop a twist or to

overcome a previously twisted state. In this scenario, it may take some period of time after the $B_y$ component has been fully introduced for sufficient torque to be applied to twist the tail. In Case et al. (2018), the effect of tail twisting became most obvious during longer timescale averages, though several tail twisting intervals were found that occurred on short timescales. We note that this result is not, however, inconsistent with the Cowley (1981) interpretation since it could indicate that the neutral sheet can twist as a result of IMF $B_y$ being introduced into the lobes only.

The excitation of a flow in the $Y$ direction ($V_y$) or in the $Y$ component of the field-perpendicular direction ($V_{\perp y}$) is linked to the introduction of the IMF $B_y$ component into the magnetotail, though it is in itself a separate effect to be studied. In the lobes, $V_y$ is introduced by asymmetric flux loading, with continued loading introducing asymmetric pressure driving convection. In the plasma sheet, on closed magnetic field lines, the differences between the Tenfjord and Cowley explanations become clear. In the Tenfjord case, one should expect rapid responses in $V_{\perp y}$. As the pressure wave from the lobes transfers through to the closed field line region, it must introduce a convective plasma flow. In the Cowley picture, however, no such pressure wave exists and instead the $B_y$ component is introduced through the Dungey cycle process. As such it takes much longer for the $B_y$ introducing field lines to propagate into the closed field line regions, where, through $\vec{E}\times\vec{B}$ drift, a $V_{\perp y}$ is introduced (e.g., Juusola et al., 2011; Pitkänen et al., 2017 and references therein).

The focus of the present study is to investigate the time it takes for the M-I system to respond to the introduction of an IMF $B_y$ component. Particularly, we investigate the response of magnetospheric and ionospheric convection to reversals in the orientation of the IMF $B_y$ component through a series of superposed epoch analyses. In the following, we undertake such analyses for the magnetospheric lobes (section 3.1), the magnetotail plasma sheet (section 3.2), and ionosphere (section 3.3).

## 2. Data

The data used in this study are collected from three separate, but linked, regions, namely, the magnetospheric lobes, the ionosphere, and the plasma sheet. Data are collated from several different magnetospheric spacecraft missions: Geotail (Nishida, 1994), Cluster (Escoubet et al., 1997), and THEMIS (Angelopoulos, 2009), along with data from the Super Dual Auroral Radar Network (SuperDARN) (Chisham et al., 2007).

Cluster's Electron Drift Instrument (EDI) (Paschmann et al., 1997) is used to study the flows within the nightside magnetotail lobes. EDI is the preferred instrument to study convection here, rather than Cluster's Ion Spectrometry (CIS) instrument (Rème et al., 2001), for example, due to the relative low density of the plasma in this region and spacecraft charging effects. We use data where the EDI instrument flags (Georgescu et al., 2010) suggest that it is working as intended (i.e., in the low-density lobe region) but further restrict data to the nightside lobes ($X_{GSM} < 0R_E$, $|Y_{GSM}| < 15R_E$, and $|Z_{GSM}| > 1R_E$) and remove flows with a velocity greater than 100 km s$^{-1}$, as these are likely to be anomalous (Haaland et al., 2008). Lobe data are also classified by hemisphere using the local $B_x$ component (i.e., $B_x > 0$ in the NH). We note that since EDI measures perpendicular drift of an electron beam gyro center, the velocity it measures is the true convection velocity, that is, $V_y \equiv V_{\perp y}$. EDI data coverage spans Years 2001–2015 inclusive for Spacecraft 1 and 3, and 2001–2004 inclusive for Spacecraft 2. No EDI data are available for Spacecraft 4.

The CIS experiment is used to determine convection within the high-density plasma sheet region where measurement errors due to spacecraft charging or low sample rates are negligible. The ion Electrostatic Analyzer (iESA) (McFadden et al., 2008) on board the THEMIS and the Low Energy Proton (LEP) instrument (Mukai et al., 1994) on board the Geotail are also used to complement the plasma sheet data from Cluster. This combined plasma sheet data set is reduced to only incorporate measurements recorded between $-50\,R_E < X_{GSM} < -14\,R_E$, $|Y_{GSM}| < 15\,R_E$, and $|Z_{GSM}| < 5\,R_E$ and with a corresponding plasma beta of greater than 0.1. Data coverage spans Years 2001–2014 for Cluster CIS (Spacecraft 1 and 3 only), 2007–2019 for THEMIS, and 1992–2016 for Geotail. All spacecraft data are resampled to 1 min resolution and are presented in GSM coordinates.

Ionospheric convection data, for Years 1999–2016 inclusive, are obtained from the SuperDARN radar network. The 35 SuperDARN radars currently in operation are used predominantly to study plasma convection in the high-latitude ionosphere in both the NH and SH (Chisham et al., 2007). In addition to the raw line-of-sight data from each radar, fitted global convection maps, produced using spherical harmonic functions via the "Map Potential" procedure, are available (Ruohoniemi & Baker, 1998). These global maps allow

the modeled plasma convection from any point in the modeled regime to be determined—even if there are no line-of-sight data in that region. This useful feature, however, makes using global maps unsuitable when looking at localized regions, as the map could have been derived from relatively few data points that are not located near the region of interest. Additionally, the global maps incorporate statistical averages that utilize the IMF $B_y$ component to derive their shape and so any flows derived from these maps would naturally respond to an IMF $B_y$ reversal.

To overcome these issues, we use a local fitting method, as described by Thomas and Shepherd (2018), to produce localized convection fits that are not dependent on large-scale statistical averages or predetermined by the orientation of the IMF. The Thomas and Shepherd (2018) method involves solving for a best fit velocity within a magnetic latitude-longitude (MLAT-MLT) cell by performing a least squares linear regression to all available line-of-sight vectors. This procedure is similar to the technique that combined instantaneous line-of-sight velocity measurements from a pair of radars with overlapping beams described by Hanuise et al. (1993). Like Thomas and Shepherd (2018), we impose a minimum azimuth separation of 25° in order to calculate a merged vector at a given location. Since we are studying the effect of IMF $B_y$ reversals on the ionospheric convection, we have far fewer intervals than Thomas and Shepherd (2018) had in their IMF-driven analysis. To further enhance the number of measurements available for our analysis, we perform the local fit to a region 8° of latitude square (i.e., a square whose sides are equal to the equivalent length of 8° of latitude at that location), such that there are anywhere up to 5,500 measurements used in each fit.

Further, we note that the size and shape of the ionospheric convection pattern is dependent upon geomagnetic activity. This introduces some uncertainty when comparing the MLAT of the flows with conjugate regions of the magnetosphere. In an effort to address this, we remove any extreme cases, such as a particularly enlarged or shrunken pattern, by restricting the SuperDARN data to intervals where the corresponding Kp index is $\geq 3$ and $<5$ (Milan et al., 2010). Additionally, we filter the data to intervals where the westward auroral electrojet index (AL) is $< -200$ nT to remove particularly strong auroral events which may suppress, or otherwise influence, the ionospheric flows.

### 2.1. IMF $B_y$ Reversals

To determine the time taken for the magnetospheric and ionospheric flows to respond to changes in the IMF $B_y$ component, we perform superposed epoch analyses with respect to IMF $B_y$ reversals. As described in Case et al. (2018), during a reversal the IMF $B_y$ state promptly switches from one orientation to the other, having both been steady before the switch and remaining steady (but oppositely orientated) after it. In this study, we simply define a reversal as having occurred if the mean IMF $B_y$ component over the 20 min period after a timestamp is oppositely directed to the 20 min mean before that timestamp. If several subsequent timestamps fulfill this criteria, the middle value of this series is taken as the reversal time. Altering the length of time we average over (e.g., 20 min) does not seem to significantly alter the number, or quality, of reversals.

Solar wind and associated IMF data, for Years 1992–2019 inclusive, are provided by the high-resolution (1 min) OMNIweb data set. These data have been time lagged to account for the propagation delay between their upstream observer (e.g., WIND, ACE, and DSCOVR) and the Earth's bow shock (King & Papitashvili, 2005). We note that, while statistically valid, individual propagation estimates can be inaccurate (e.g., Case & Wild, 2012; Mailyan et al., 2008; Vokhmyanin et al., 2019). Additionally, the time taken for the shocked solar wind to traverse from the bow shock to the magnetopause is variable and is not accounted for in the OMNI data set. Since we do not attempt to account for this extra delay either, we expect that any responses to the IMF $B_y$ reversals will be offset by 5 to 15 min (Khan & Cowley, 1999).

From the OMNI data set, a subset of 5,767 positive to negative IMF $B_y$ reversals are found, and a set of 5,798 negative to positive reversals. In the following analyses, observations from the magnetosphere and ionosphere contemporaneous data to these reversals are collated and averaged. We note that not all of the IMF $B_y$ reversals have coincident spacecraft or ionospheric data, due to the data coverage of those data sets and the suitability of the spacecraft locations.

## 3. Results

### 3.1. Lobe Flows

Plotted in Figure 1 is a superposed epoch analysis of the convection velocity in the nightside magnetotail lobes, as recorded by Cluster's EDI instruments. Data recorded from 30 min before an IMF $B_y$ reversal and

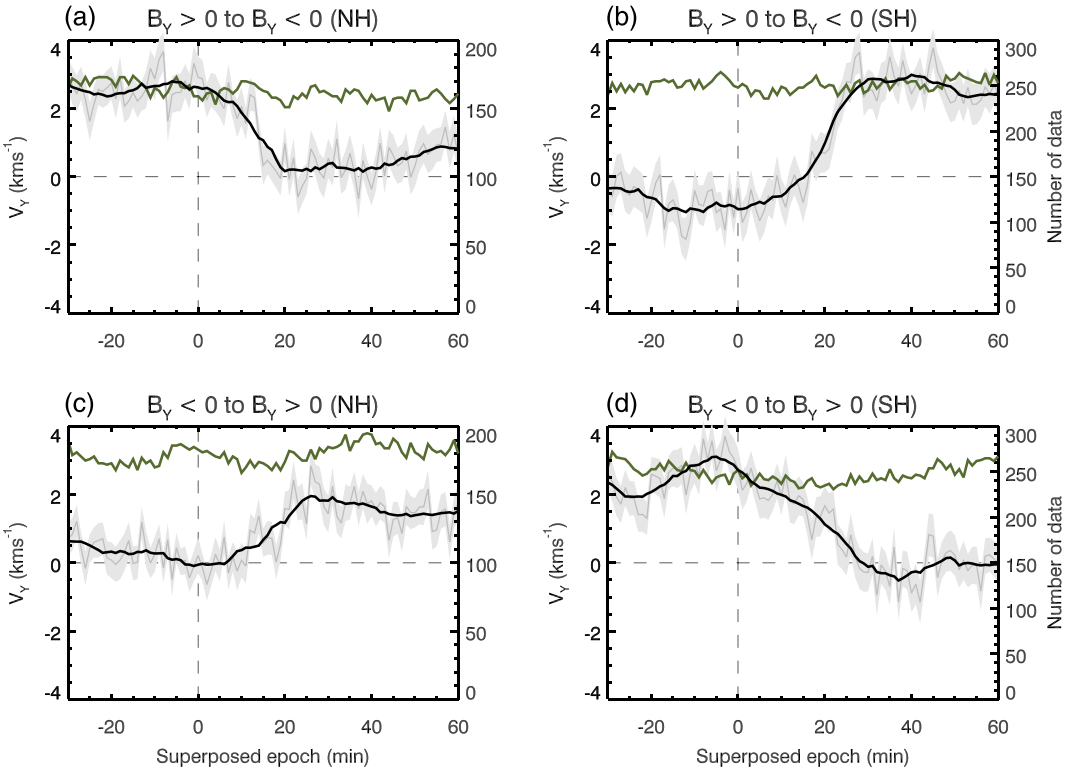


**Figure 1.** Superposed epoch Cluster-EDI velocity data sampled in the lobes are shown for (a and b) IMF $B_y$ positive to negative reversals and for (c and d) IMF $B_y$ negative to positive reversals. (a and c) Northern Hemisphere (NH) and (b and d) Southern Hemisphere (SH) data are shown, respectively. Plotted in black are the smoothed superposed means for all data. The gray line shows the unsmoothed means, and the gray shaded regions indicate the standard error of the mean for each timestamp. The number of data points for each superposed average timestamp is shown by the olive green line on the secondary *y* axis.

up to 60 min after a reversal are temporally aligned and their mean is computed. In panels (a) and (b), the data correspond to a positive to negative IMF $B_y$ reversal and were collected in the NH and SH, respectively. In panels (c) and (d), the data correspond to a negative to positive IMF $B_y$ reversal.

Shown by the thin gray line is the mean for each superposed timestamp. The gray shaded region indicates the standard error of that mean. Plotted with a thick black line are the smoothed means (10-point moving average centered on the timestamp). Plotted in olive green, and shown on the secondary *y* axis, are the number of data points that went into each time step average.

Plotted in Figure 1a is a superposed epoch analysis of lobe flows in the NH with respect to positive to negative IMF $B_y$ reversals. The average $V_y$ flow is positive, remaining steady around +2.5 km s$^{-1}$ until the IMF $B_y$ reverses orientation. The average $V_y$ flow decreases, though does not quite become negative, after the IMF $B_y$ reversal and reaches a minimum state between 20 and 30 min.

In panel (b), a superposed epoch analysis is shown for the same IMF $B_y$ reversal type as panel (a) but with data from the SH. The trend is broadly opposite to that shown in panel (a), with an average $V_y$ of around −1 km s$^{-1}$ under positive IMF $B_y$, steadily increasing after the reversal to around +3 km s$^{-1}$ under negative IMF $B_y$. Again, the $V_y$ flows reach a maximum state around 30 min after the reversal occurs.

Panel (c) is again for $V_y$ data in the NH lobe, though this time associated with an IMF $B_y$ negative to positive reversal. Its trend is almost opposite to the trend in panel (a) (i.e., opposite IMF $B_y$ reversal type but same hemisphere) and broadly the same as the trend in panel (b) (i.e., opposite reversal type and opposite hemisphere). The average $V_y$ lobe flow is around 0 under negative IMF $B_y$ steadily increasing to around +2 km s$^{-1}$ under positive IMF $B_y$, with this maximum being reached around 30–40 min after the reversal occurs.

In panel (d), $V_y$ data from the SH for the IMF $B_y$ negative to positive reversal are shown. Its trend is almost exactly opposite to that in panel (b) (i.e., opposite IMF $B_y$ reversal type but same hemisphere) and broadly

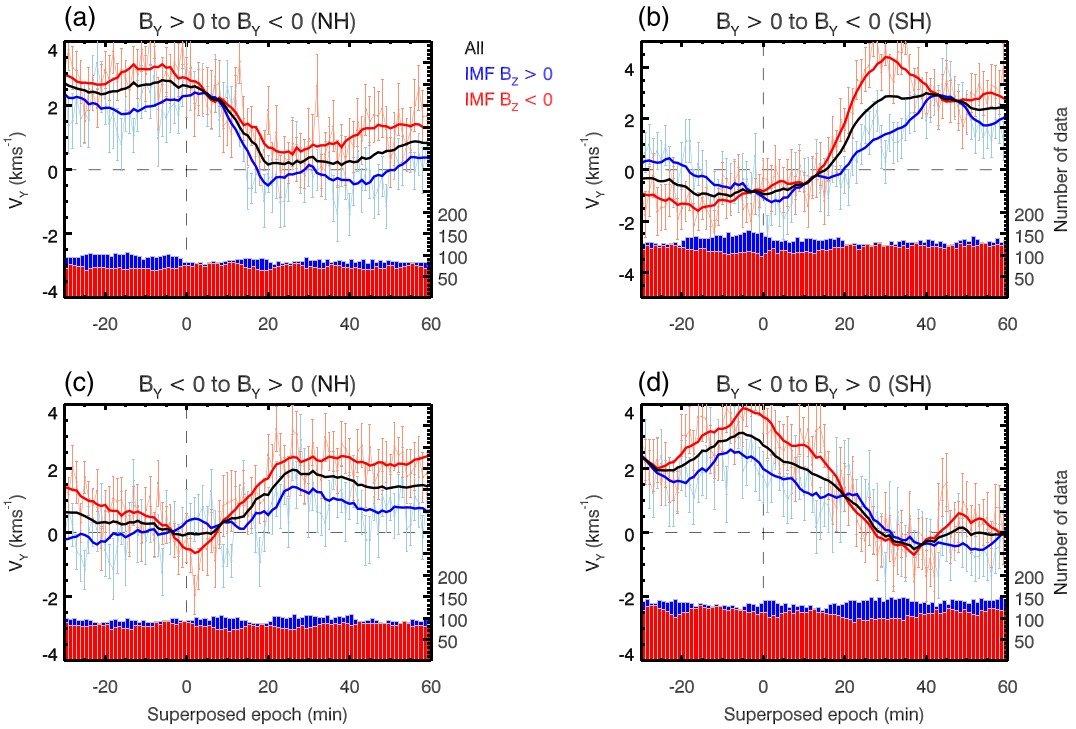


**Figure 2.** In the same format as Figure 1, superposed epoch Cluster-EDI velocity data sampled in the lobes are shown for (a and b) IMF $B_y$ positive to negative reversals and for (c and d) IMF $B_y$ negative to positive reversals. (a and c) Northern Hemisphere (NH) and (b and d) Southern Hemisphere (SH) data are shown, respectively. Plotted in blue and red are data for positive and negative IMF $B_z$, respectively.

the same as the trend in panel (a) (i.e., opposite reversal type and opposite hemisphere). The average lobe $V_y$ flow is around +2 km s$^{-1}$ under negative IMF $B_y$ and steadily decreases to around −1 km s$^{-1}$ 30 min after the reversal occurs.

From the above plots, we also note a persistent asymmetry, with a generally positive $V_y$. We also note slightly different $V_y$ magnitude changes between the NH and SH, as well as differences between positive to negative and negative to positive IMF $B_y$ reversals. A detailed study of these features is beyond the scope of the present paper, but differences in the magnetospheric response between IMF $B_y > 0$ and IMF $B_y < 0$ states have been discussed recently (e.g., Holappa & Mursula, 2018; Liou et al., 2020; Reistad et al., 2020).

### 3.1.1. IMF $B_z$ Dependence

In the following, the lobe flows presented in Figure 1 have been further split based upon the 30 min median IMF $B_z$. Additionally, to account for the fact that the IMF $B_z$ orientation may also reverse alongside the IMF $B_y$ orientation, we require that 80% of data that make up the average match the sign of the average. In Figure 2, the superposed epoch of flows with an associated positive median IMF $B_z$ is plotted with the blue line and negative IMF $B_z$ with the red line. The red and blue "error bars" show the standard errors of the mean of each timestamp average and the black line shows the mean for all data. The red and blue histograms show the total amount of data for their respective classifications.

In general, the IMF $B_z$ orientation alone appears to have little effect on the overall trends, with changes in the direction of the lobe $V_y$ being consistent regardless of IMF $B_z$.

### 3.1.2. Solar Wind Speed Dependence

We have also split the lobe flows presented in Figure 1 based upon the 30 min median solar wind velocity $V_{sw}$. In Figure 3, the superposed epoch of flows with an associated median $V_{sw} < 450$ km s$^{-1}$ ("slow") is plotted with the blue line and $V_{sw} \geq 450$ km s$^{-1}$ ("fast") with the red line. The red and blue "error bars" show the standard errors of the mean of each timestamp average, and the black line shows the mean for all data. The red and blue histograms show the total amount of data for their respective classifications.

As with the IMF $B_z$ orientation, it appears that the solar wind velocity alone has little affected on the overall trends, with changes in the direction of the lobe $V_y$ being largely consistent for both fast and slow $V_{sw}$.

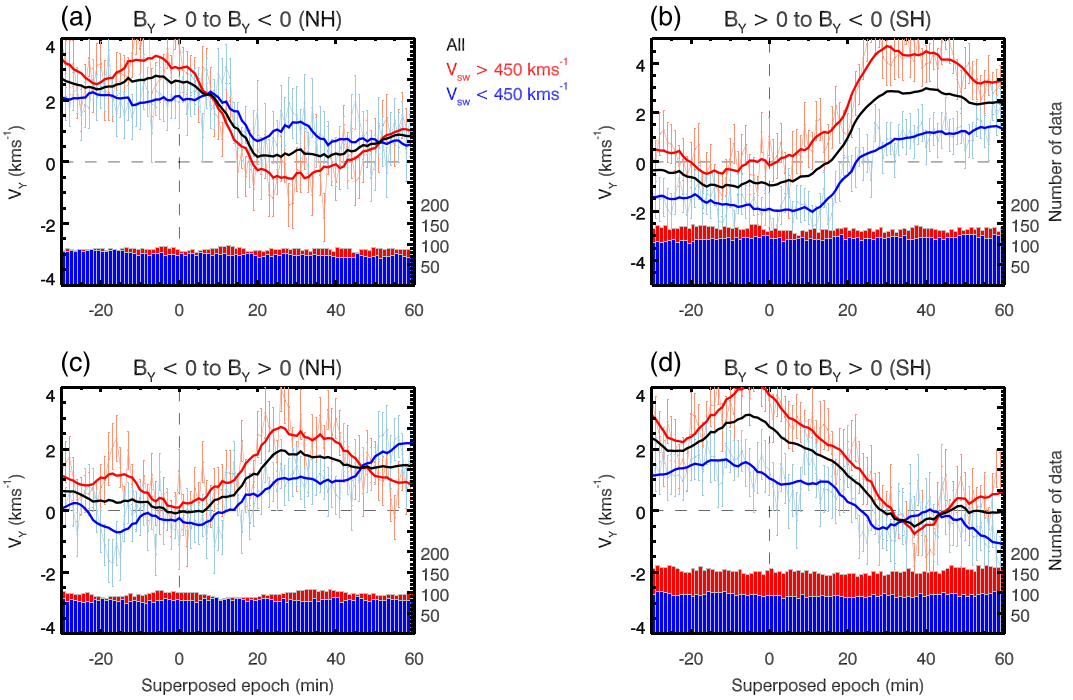


**Figure 3.** In the same format as Figure 1, superposed epoch Cluster-EDI velocity data sampled in the lobes are shown for (a and b) IMF $B_y$ positive to negative reversals and for (c and d) IMF $B_y$ negative to positive reversals. (a and c) Northern Hemisphere (NH) and (b and d) Southern Hemisphere (SH) data are shown, respectively. Plotted in blue and red are data for $V_{sw} < 450$ km s$^{-1}$ and $V_{sw} \geq 450$ km s$^{-1}$, respectively.

However, the lobe $V_y$ flows are, in general, more consistently displaced toward positive $V_y$ for fast solar wind when compared with slow solar wind. The only exception to this is in panel (a), under negative IMF $B_y$, where the lobe flows associated with fast solar wind average around −0.5 km s$^{-1}$, while the flows associated with slow solar wind average around +1 km s$^{-1}$.

### 3.1.3. Dayside Reconnection Rate Dependence

The response of the magnetospheric system, including the lobes, to upstream driving is governed by a combination of factors—rather than just the solar wind velocity and IMF $B_z$ previously analyzed. To combine these two factors, however, is nontrivial. Slow solar wind may still be geoeffective if accompanied by a strongly negative $B_z$. Conversely, a weakly negative IMF $B_z$ may be geoeffective with a strong solar wind velocity. We therefore utilize the dayside reconnection parameter, $\Phi_D$, of Milan et al. (2012) to better combine the effects of these two parameters.

Milan et al. (2012) define the dayside reconnection rate, $\Phi_D$, as the magnetic flux per unit of time converted from a closed topology to open topology, measured in volts. Specifically, through their statistical analysis of the rate of growth of the auroral oval, they determine the following expression for $\Phi_D$ :

$$\Phi_D = L_{eff}(V_x) V_x B_{yz} \sin^{9/2}\left(\frac{|\theta|}{2}\right) \quad (1)$$

where

$$L_{eff}(V_x) = 3.8 R_E \left(\frac{V_x}{4 \times 10^5 \text{m s}^{-1}}\right) \quad (2)$$

and $B_{yz} = \sqrt{{B_y}^2 + {B_z}^2}$ and $\theta = \tan^{-1}\left(\frac{B_y}{B_z}\right)$.

In Figure 4 we have split the lobe flows presented in Figure 1 based upon the dayside reconnection rate $\Phi_D$. The superposed epoch of flows with an associated $\Phi_D < 90$ kV is plotted with the blue line and $\Phi_D > 100$ kV with the red line. The red and blue "error bars" show the standard errors of the mean of each timestamp average, and the black line shows the mean for all data. The red and blue histograms show the total amount of data for their respective classifications.

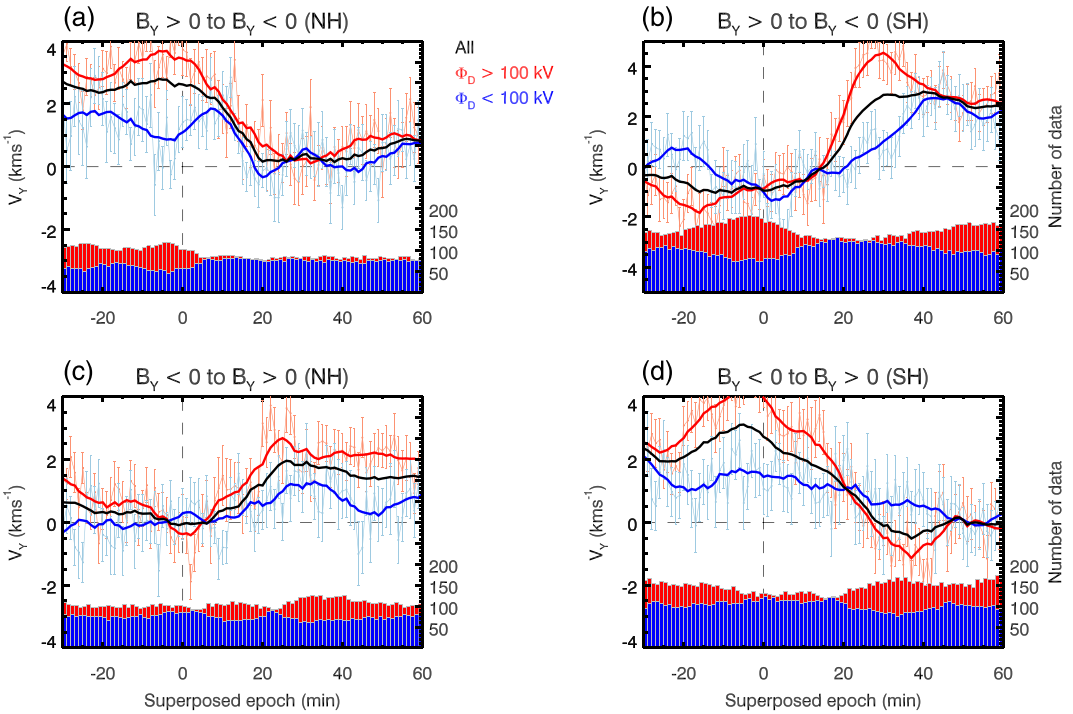


**Figure 4.** In a similar format as Figure 1, superposed epoch Cluster-EDI velocity data sampled in the lobes are shown for (a and b) IMF $B_y$ positive to negative reversals and for (c and d) IMF $B_y$ negative to positive reversals. (a and c) Northern Hemisphere (NH) and (b and d) Southern Hemisphere (SH) data are shown, respectively. Plotted in blue and red are data for $\Phi_D < 100$ kV and $\Phi_D > 100$ kV, respectively. The number of data points for each subset is shown by the histogram bars.

For enhanced dayside reconnection rates, that is, $\Phi_D > 100$ kV (red line in Figure 4), we see a clear reversal in the lobe flow $V_y$ component associated with the IMF $B_y$ orientation. The trend is broadly similar to that shown in Figure 1, with distinct reversals in the flow direction starting almost immediately after a reversal and being complete within around 30 min.

For decreased dayside reconnection rates, that is, $\Phi_D < 100$ kV (blue line in Figure 4), we do not see such a clear response. The $V_y$ flows are, in general, more suppressed than their enhanced counterparts and their response is less distinct and more gradual.

### 3.2. Plasma Sheet Flows

Data from the Cluster CIS, Geotail LEP, and THEMIS iESA instruments are selected to provide flow data in the plasma sheet region ($-50 < X_{GSM} < -14\,R_E$, $|Y_{GSM}| < 7\,R_E$, $|Z_{GSM}| < 3\,R_E$) with a corresponding plasma beta greater than 0.1. The flow data are then further restricted to intervals of earthward flow ($V_x > 0$ km s$^{-1}$) since tailward flow, predominantly the result of reconnection events, would be expected to occur in the opposite $Y$ direction. Additionally, flows with a total velocity greater than 500 km s$^{-1}$ are removed, as these are likely to be traveling too fast to be directly affected by any induced IMF $B_y$ effects (Juusola et al., 2011).

A superposed epoch analysis of the plasma sheet flows is presented in Figure 5, with the same format as Figure 1, though extended up to 4 hr after an IMF $B_y$ reversal. In panels (a) and (b), the plotted data correspond to a positive to negative IMF $B_y$ reversal and were collected in the NH and SH, respectively. Since the neutral sheet is not stationary and does not necessarily lie on the $Z_{GSM} = 0$ axis, we use the $B_x$ component of the local magnetic field to define whether the data are in the NH or SH. In panels (c) and (d), the plotted data correspond to a negative to positive IMF $B_y$ reversal. The number of data points for each averaged timestamp is shown by the olive green line on the secondary $y$ axis.

The results of the superposed epoch analyses for the plasma sheet are much less clear than those for the lobes. On a short timescale, we see a reversal from $V_y$ around −10 to +30 km s$^{-1}$ in panel (a), occurring within 30 min of the reversal. Additionally, in panel (c) (same hemisphere as panel a but opposite IMF $B_y$

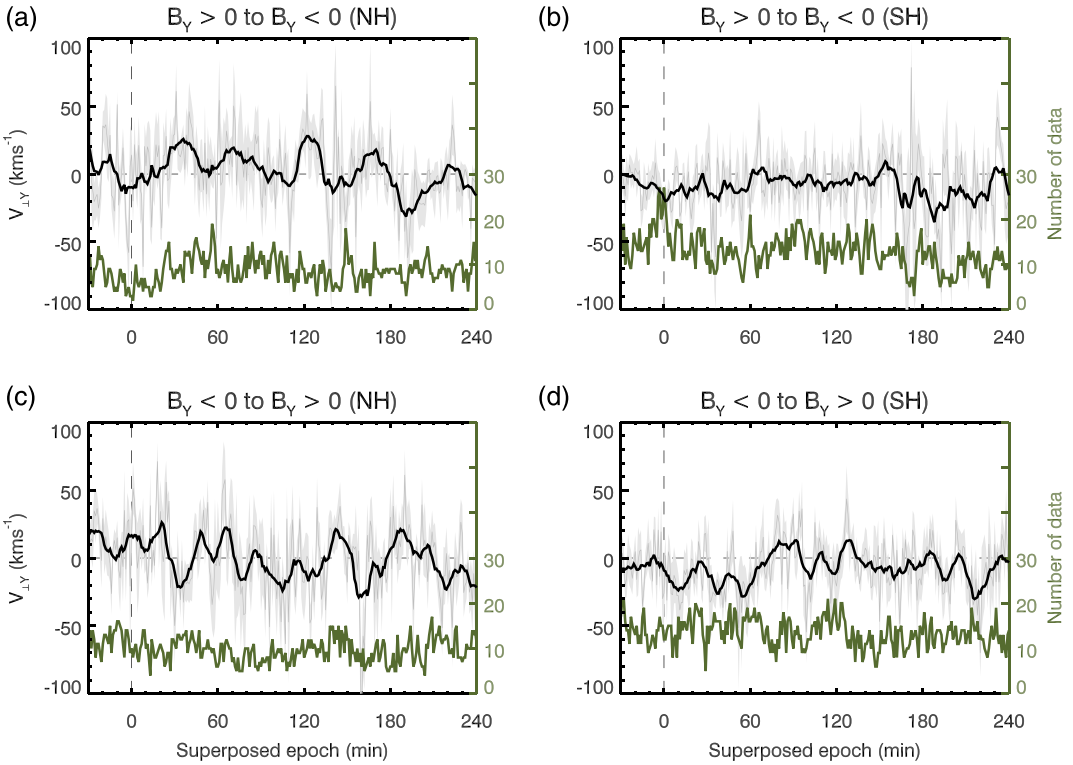


**Figure 5.** Superposed epoch plasma sheet velocity data are shown for (a and b) IMF $B_y$ positive to negative reversals and for (c and d) IMF $B_y$ negative to positive reversals. (a and c) Northern Hemisphere (NH) and (b and d) Southern Hemisphere (SH) data are shown, respectively. Plotted in black are the superposed means for all data. The gray shaded region indicates the standard error of the mean for each timestamp. The number of data points for each superposed average timestamp is shown by the olive green line on the secondary *y* axis.

reversal) we see the opposite occur, with $V_y$ starting at around +20 km s$^{-1}$ and finishing reaching −20 km s$^{-1}$ at around 30 min of the reversal.

However, the reversals observed are of the same order as subsequent variations throughout the complete 4 hr window. Additionally, corresponding reversals are not observed in the SH.

### 3.3. Ionospheric Flows

Convection in the ionosphere is intrinsically coupled to the convection of magnetic flux in the magnetosphere. Ionospheric flows, therefore, provide another way of measuring the large-scale convection of the magnetotail. As such, we utilize the SuperDARN radar network to determine the corresponding ionospheric flows for the lobes and plasma sheet regions. In the panels of the following figures, we present superposed epoch analyses of the best fit velocities from the SuperDARN radar network for 8° intervals in MLAT, spanning from 60° MLAT in the dayside ionosphere along the noon-midnight meridian and across the polar cap to 60° MLAT in the nightside ionosphere. Data are from the NH network only, which generally provides significantly better coverage than the SH network particularly at lower latitudes. As mentioned in section 2, the data are filtered to intervals of $3 \leq Kp < 5$ and $AL < -200$ nT to remove active periods.

Data corresponding to a positive to negative IMF $B_y$ reversal are shown in Figure 6, and data corresponding to a negative to positive reversal are shown in Figure 7. In both figures the average flow direction ($\theta$) and magnitude ($|V|$) are shown by the blue and red lines, respectively. The flow direction is determined by taking the tangent of the average east and north components of the measured vectors (i.e., where $\theta = 90°$ is eastward flow and $\theta = -90°$ is westward) and is completely independent of any large-scale fits or predetermined convection patterns. We note that the average flow direction reverses over the pole as a result of the sign of $v_{North}$ changing. The number of data points in each averaged time stamp is shown by the gray line on the secondary axis.

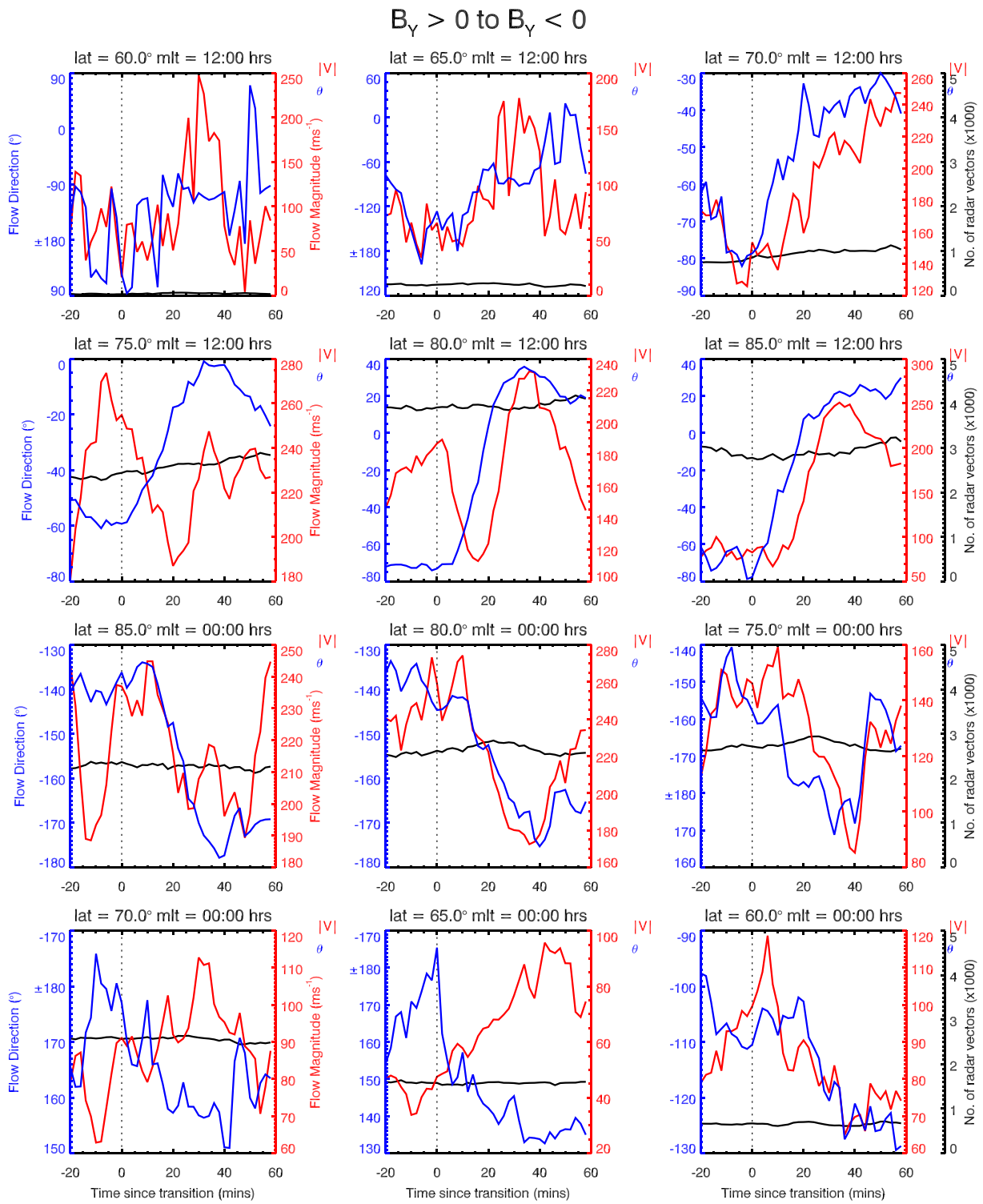


**Figure 6.** Superposed epoch SuperDARN ionospheric flows, recorded in the Northern Hemisphere, along the noon-midnight meridian (MLT) across the polar cap from 60° MLAT on the dayside to 60° MLAT on the nightside. Data correspond to a positive to negative IMF $B_y$ reversal. Plotted in red is the median flow speed, and in blue is the median flow direction. The number of vectors for each superposed average time stamp is shown by the black line on the secondary axis. The secondary axis has been scaled down by 1,000, that is, 5 = 5,000 vectors.

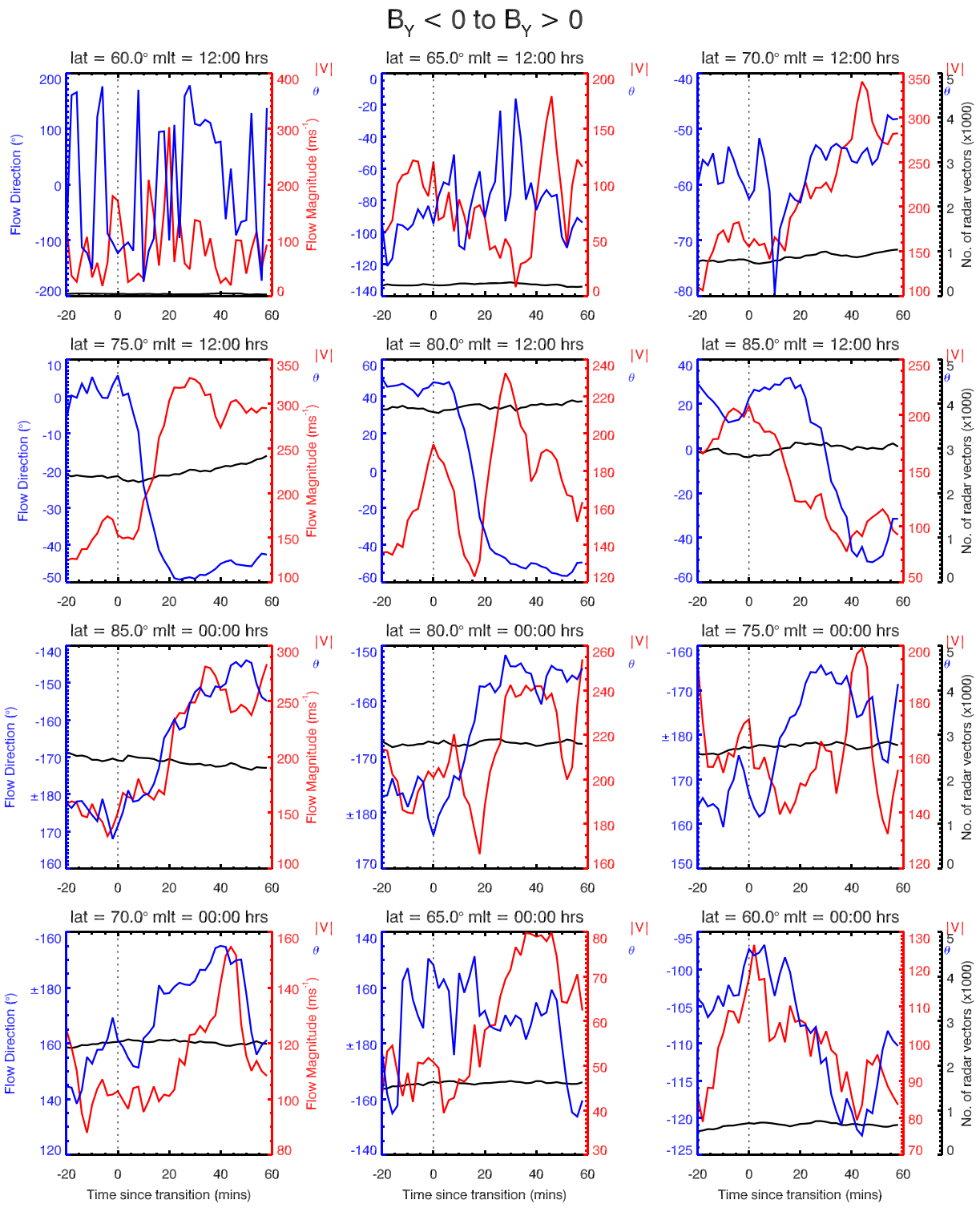


**Figure 7.** As Figure 6 but with superposed epoch SuperDARN ionospheric flows corresponding to a negative to positive IMF $B_y$ reversal.

The ionosphere poleward of 75° MLAT, where the field lines are predominantly open, clearly responds to reversals in the IMF $B_y$ orientation. For positive to negative IMF $B_y$ reversals, the ionospheric flows are directed more eastward (i.e., toward 90°). Conversely, for negative to positive IMF $B_y$ reversals the ionospheric flows are directed more westward (i.e., toward −90°). For example, compare the 80° MLAT on the dayside (12 MLT) panels during the two types of IMF $B_y$ reversal. During a positive to negative reversal (Figure 6), the flow orientation is steady at −70° during the positive IMF $B_y$ interval, before rapidly changing direction to +40° around 30 min after the $B_y$ reversal. During a negative to positive reversal (Figure 7), flow orientation is steady at +45° during the negative IMF $B_y$ interval, before rapidly changing direction and reaching −50° around 30 min after the $B_y$ reversal.

Equatorward of 75°, that is, closed field lines that map to the plasma sheet region of the magnetosphere, the response is less clear. In some cases, a response consistent with the higher latitudes does seem evident (e.g., 65° and 70° MLAT at 1200 MLT in Figure 6); however, in other cases no response is evident (e.g., 65° and 70° MLAT at 1200 MLT in Figure 7). At 60° MLAT on the dayside, for both reversal types, the flows are incredibly variable suggesting the IMF $B_y$ has no direct control on the flows in this region.

As with the lobe data, the response time of the ionospheric flows, in the open field line region, to an IMF $B_y$ reversal is prompt. Flows start to change direction within 10–15 min and have completed their response, reaching a new end state, within 30–40 min.

## 4. Discussion

In this study, we have shown that the magnetotail lobes, in which the field lines are connected to the IMF, respond promptly to reversals in the IMF $B_y$ component. In the plasma sheet, where the field lines are closed, the picture is more complex with no obvious response to IMF $B_y$ reversals. In the ionosphere, we find clear responses in the flow direction at higher latitudes but a less clear response at latitudes below 75° MLAT.

When analyzing how specific events or phenomena in the M-I system are driven by the IMF, previous studies have tended to either use or find an interval of IMF for which the average state best matches their results. The length of this interval has varied from study to study. For example, Juusola et al. (2011) used an IMF averaging time of 30 min when studying plasma sheet convection and work by Tenfjord et al. (2015, 2017) has suggested that the nightside magnetosphere could respond to changes in the IMF $B_y$ orientation on timescales as short as 15 min. However, longer timescales have also been suggested. For example, Fear and Milan (2012) found an average of the IMF $B_y$ component 3–4 hr previously best matched the local time of transpolar arc formation, and Browett et al. (2017) found that the $B_y$ component in the tail best correlated with IMF conditions on timescales of 1.5 and 3 hr, depending on solar wind conditions.

In a statistical study of "fast flow" events in the plasma sheet, Pitkänen et al. (2013) investigated the effect of different time averaging on their correlations and found a 130 min average of the IMF $B_y$ preceding their fast flows resulted in the highest correlation with their data. They also noted, however, that their correlations were generally high, regardless of averaging length chosen, and attributed this to the stability of the IMF $B_y$ component (e.g., Borovsky, 2008; Milan et al., 2010). However, in a later study investigating "slow flows," Pitkänen et al. (2019) use a 15 min average taken 135 min prior to the corresponding data measurement in the tail. They cite the result of Petrukovich and Lukin (2018), who developed a linear regression model of the plasma sheet $B_y$ component with respect to the IMF $B_y$ component using Geotail data, as justification for this.

Of course, these studies all investigated different effects that can be introduced by an IMF $B_y$ component. It is therefore entirely possible that the responses of these separate effects will occur on different timescales. However, it still leaves the question of what time should we average over when analyzing events in the magnetotail that are driven by the IMF $B_y$ component or, perhaps critically, whether averaging over some interval is appropriate at all, particularly when the IMF $B_y$ component may have remained steady over many hours before the event occurs.

To help address this, in this study, we have specifically investigated intervals of IMF $B_y$ reversals to remove any potential ambiguity in the response timings of convection due to the stability effect of the IMF $B_y$ component. During a reversal, the IMF $B_y$ component swaps orientation (e.g., $B_y > 0$ to $B_y < 0$) having been both steady before the reversal and remaining so afterward (Case et al., 2018).

We note that, in the Tenfjord explanation, the rationale for a prompt introduction of the IMF $B_y$ into the magnetotail is magnetic tension forces inducing shear flows, in the opposite direction to the untwisting flows commonly studied when examining asymmetric magnetospheric dynamics (e.g., Grocott et al., 2007; Pitkänen et al., 2013; Reistad et al., 2018), on the inner magnetosphere creating a twist on the field lines. Indeed, Tenfjord et al. (2018) note that in their magnetohydrodynamic (MHD) modeling, the inner magnetosphere ($X = -6.7\,R_E$) responds first with the effect then propagating downtail (to a minimum of $X = -11\,R_E$ in their study). This suggests that $V_y$ and $V_{\perp y}$ should also respond on short timescales. Although the Cowley explanation does suggest a prompt response in the lobes, it also suggests longer timescales in the plasma sheet. Indeed, with the Cowley explanation, the IMF $B_y$ component is introduced into the tail as the result of the Dungey cycle and so, in this case, both the $B_y$ and $V_{\perp y}$ response would propagate from downtail to the inner nightside magnetosphere, such as found by Pitkänen et al. (2016).

In Figure 1, we analyze the response of the flows in the magnetotail lobes to reversals in the IMF $B_y$ component. The figure demonstrates that the $Y$ direction of flow in the lobes is dependent upon the IMF $B_y$ orientation. In the NH, positive IMF $B_y$ driving results in positive $V_y$ on average and negative IMF $B_y$ driving results in negative $V_y$ on average. This general trend is reversed in the SH. This result is consistent with our understanding of the asymmetric flux loading in the lobes (e.g., Cowley, 1981; Cowley & Lockwood, 1992). For example, both Haaland et al. (2008) and Case et al. (2018) have previously shown how the lobe flows are directed with respect to the IMF $B_y$ orientation through in situ convection measurements. In both these studies, the average IMF $B_y$ direction was used to classify the upstream conditions corresponding to each lobe flow. However, as previously noted, in this study we have instead looked at lobe flows explicitly associated with IMF $B_y$ reversals.

This important distinction allows us to determine the response time of the lobe flows to changes in upstream driving, particularly in reversals of the orientation of the IMF $B_y$ component. As shown in Figure 1, the flows start responding promptly (<5 min) to reversals in the IMF $B_y$ orientation and reach an equilibrium or "end state," based on the new orientation, within 30–40 min. We note that there is some inherent uncertainty in such an analysis since our zero-epoch value, that is, when the IMF $B_y$ reversal occurs, is not measured directly but is instead taken from the OMNI data set which has been time shifted to the bow shock rather than to the interaction region at the dayside magnetopause.

A prompt response in the magnetotail lobes is to be expected for both the Tenfjord and Cowley mechanisms. Although we do not place any criteria on the orientation of the IMF $B_z$ component, in Figure 1, we still expect that at least some reconnection between the IMF and magnetopause will occur, even if under northward IMF conditions (e.g., Kessel et al., 1996), and that the resultant newly opened field lines will quickly propagate across the polar cap (e.g., Dungey, 1961). Additionally, previous studies such as Tenfjord et al. (2018) have shown that there is little difference in response times for the introduction of a $B_y$ component for northward or southward IMF intervals in the inner magnetosphere. Indeed, when we split the Cluster EDI convection data by IMF $B_z$ orientation, as shown in Figure 2, we found little difference in the response times. This was also true when we split by solar wind velocity—as shown in Figure 3. However, when we split by dayside reconnection rate, we did see a clear difference between the response of high and low reconnection rates. This indicates that it is the electromagnetic (e.g., Poynting flux), rather than kinetic, energy of the solar wind and IMF that controls the lobe flows. We note that this prompt response of the lobes follows for both the Cowley and the Tenfjord explanations for introducing a $B_y$ component (and hence exciting $V_y$ flows) into the tail, as they both rely on IMF-magnetopause reconnection creating an asymmetric flux loading of the lobes.

Although it is clear that flows in the lobe region of the magnetotail are quick to respond to changes in the IMF $B_y$ orientation, results from the plasma sheet are much less clear. As shown in Figure 5, no significant trends are found for the flows in the plasma sheet in relation to the reversal of the IMF $B_y$ orientation. This appears to be in contrast to other studies, such as Grocott et al. (2007), Juusola et al. (2011), and Pitkänen et al. (2013, 2017), who have demonstrated the existence of asymmetries in the plasma sheet flows based on the IMF $B_y$ orientation. Additionally, it appears to be in contrast to both the Cowley (Cowley, 1981; Cowley & Lockwood, 1992) and the Tenfjord (Tenfjord et al., 2015, 2017) explanations for $V_y$ flows being excited in the magnetotail. With the Tenfjord explanation, we should see a response in the plasma sheet on timescales of 30–40 min. With Cowley explanation, we should see a response on the order of several hours—since the introduction of a flow asymmetry on closed plasma sheet field lines requires the complete Dungey cycle convection of IMF field lines.

We note that the number of data points presented in Figure 5 is low. Requiring that a spacecraft is located within the exact region of interest around the time of an IMF $B_y$ reversal is a difficult criterion to fulfill. Therefore, to validate these magnetospheric findings, we complement the in situ spacecraft data with ionospheric flow data recorded by the SuperDARN radars. Since the ionospheric flows are intrinsically tied to, though not necessarily constrained by, the convection of magnetic field lines in the magnetosphere, they provide an additional data source to investigate the response of the M-I system to reversals in the IMF $B_y$ component.

In Figures 6 and 7, we present the ionospheric flows recorded by the SuperDARN radar network. We note that, as described in section 2, these flows are the best fit velocities derived directly from the radar line of sight velocity measurements, rather than estimates from the global best fit Map Potential patterns often used. At ≥75° MLAT, with field lines mapping out into the lobes, clear responses in the flow direction can be seen to the reversal in IMF $B_y$ orientation—matching the data recorded by the in situ spacecraft. However, at <75° MLAT, mapping out to the plasma sheet region, the response is much less clear for both reversal types. In some instances, a response consistent with higher latitudes does appear, though is somewhat weaker, while in other cases no clear response is seen at all. Data coverage does not appear to be an issue here, with over 1,000 data points for each superposed epoch interval. We therefore believe that we can rule out data coverage as a potential explanation for the apparent discrepancy between past studies and the plasma sheet results presented here.

We believe that the lack of response observed in the plasma sheet, and its apparent disagreement with previous studies, for example, Juusola et al. (2011) and Pitkänen et al. (2016), could, in fact, be explained by the Dungey cycle. For example, in the Cowley explanation (Cowley, 1981; Cowley & Lockwood, 1992) of introducing a $B_y$ component into the magnetotail, tail reconnection is needed to drive the introduced $B_y$ field from the lobes into the near-Earth plasma sheet. Tail reconnection is a pseudorandom event meaning that when performing superposed epoch analyses, such as ours, its effects would be smeared out—leading to no discernible result. Yet when one specifically looks for these $B_y$-related flows in the tail, for example, Pitkänen et al. (2016), the reconnection event must have already taken place for the flows to be observed and thus the control is clear. Importantly, we also note that too much tail activity, particularly substorms, can inhibit the asymmetry observed in ionospheric flows (e.g., Ohma et al., 2018, 2019; Reistad et al., 2018) and so we have attempted to address this by filtering by *Kp* and *AL* in the SuperDARN plots.

We note that our plasma sheet flow data is sampled between −14 and −50 $R_E$, which is significantly further downtail than the data and modeling used by Tenfjord et al. (2015, 2017, 2018). It may be that we simply do not see the prompt reversal response further downtail due to the complex nature of the magnetotail or that this explanation does not hold outside of the near-Earth region discussed in Tenfjord et al. (2018). Additionally, we are analyzing convection data, rather that the magnetic field data, and there is the potential for differences here (e.g., the convection data is a mix of a $B_y$ component being introduced and undone from a previous IMF $B_y$ state).

## 5. Conclusions

The orientation of the IMF $B_y$ has previously been shown to exert an influence on the direction of the convection in the magnetotail lobes. Using two complementary data sets, from in situ spacecraft and ionosphere radars, we confirm that a positive IMF $B_y$ component drives, on average, positive-$Y_{GSM}$-directed flows in the NH while a negative IMF $B_y$ component drives negative-$Y_{GSM}$-directed flows. This trend is reversed in the SH. We note that a flow in the positive-$Y_{GSM}$ direction corresponds to an eastward flow ($\theta = 90°$) in the dayside ionosphere but a westward flow ($\theta = -90°$) in the nightside ionosphere.

We utilize superposed epoch analyses of flow data from the lobes, plasma sheet, and ionosphere to rigorously investigate the timing of the M-I system's response to changes in the IMF $B_y$ component. Particularly, we identified convective flows from these regions that were associated with IMF $B_y$ reversals to determine how quickly the direction of these flows changed in response to a reversal in the IMF $B_y$ orientation.

We found that the average flows in the lobes respond promptly to a reversal in the IMF $B_y$ component, with the flow direction starting to change within 5 min of the IMF $B_y$ reversals seen in the OMNI data. The average flows reverse in direction around 30–40 min after the IMF $B_y$ reversal. Additionally, we found that the dayside reconnection rate seems to influence how the lobes respond, with larger reconnection rates

($\Phi_D > 100$ kV) producing clearer results than smaller rates. Clear and prompt responses were also found with the ionospheric flows at latitudes mapping out to the lobe region (≥75°MLAT), suggesting that changes in the lobes are introduced into the polar cap ionosphere almost instantly. However, in our superposed epoch analyses, the plasma sheet did not respond to reversals in the IMF $B_y$ component on the timescales used in this study (up to 4 hr after a reversal). The responses of the associated ionospheric convection data, at 60–70° MLAT, were also less clear than their higher-latitude counterparts.

Our result of a prompt response to reversals in the lobes is consistent with both the Cowley and Tenfjord explanations for introducing a $B_y$ component (and subsequently $V_y$) into the closed field line tail. At first glance, the null result in the plasma sheet appears to be inconsistent with both explanations. However, it is possible that it may actually be consistent with the Cowley explanation due to the nature of the reconnection-driven Dungey cycle complicating any superposed epoch analysis such as ours. Further investigation into the role of tail reconnection adding the IMF $B_y$ component into the inner magnetotail is needed.

## Data Availability Statement

The Cluster data were provided by ESA's Cluster Science Archive (https://www.cosmos.esa.int/web/csa). The Geotail data are provided from the Data ARchives and Transmission System (DARTS) of the Institute of Space and Astronautical Science (https://www.darts.isas.jaxa.jp/stp/geotail/data.html). The THEMIS data were provided by NASA Goddard Space Flight Center's CDAWeb (https://cdaweb.sci.gsfc.nasa.gov/). Solar wind data were provided by NASA GSFC's OMNIWeb database (https://omniweb.gsfc.nasa.gov/).

**Acknowledgments**
We gratefully acknowledge the various instrument teams from each of the spacecraft missions used in this study. The authors acknowledge the use of SuperDARN data. SuperDARN is a collection of radars funded by national scientific funding agencies of Australia, Canada, China, France, Japan, South Africa, United Kingdom, and the United States, and we thank the international PI team for providing the data. The authors acknowledge access to the SuperDARN database (http://bslsuperdarnc.nerc-bas.ac.uk:8093/docs/) and the Radar Software Toolkit that is used to process the data (https://zenodo.org/record/1403226#.Xy0u7y3MxTY). N. A. C. and A. G. were supported during this study by STFC Grant ST/R000816/1. R. C. F. was supported by STFC Consolidated Grant ST/R000719/1. S. H. acknowledges support from the Norwegian Research Council under Grant 223252. J. H. L. was supported by an FST studentship from Lancaster University.

## References

Angelopoulos, V. (2009). The THEMIS mission. In J. L. Burch & V. Angelopoulos (Eds.), *The THEMIS mission* (pp. 5–34). New York, NY: Springer New York.

Blanc, M. (1988). Magnetosphere-ionosphere coupling. *Computer Physics Communications*, *49*(1), 103–118. https://doi.org/10.1016/0010-4655(88)90219-6

Borovsky, J. E. (2008). Flux tube texture of the solar wind: Strands of the magnetic carpet at 1 AU? *Journal of Geophysical Research*, *113*, A08110. https://doi.org/10.1029/2007JA012684

Browett, S. D., Fear, R. C., Grocott, A., & Milan, S. E. (2017). Timescales for the penetration of IMF $B_y$ into the Earth's magnetotail. *Journal of Geophysical Research: Space Physics*, *122*, 579–593. https://doi.org/10.1002/2016JA023198

Case, N. A., Grocott, A., Haaland, S., Martin, C. J., & Nagai, T. (2018). Response of Earth's neutral sheet to reversals in the IMF $B_y$ component. *Journal of Geophysical Research: Space Physics*, *123*, 8206–8218. https://doi.org/10.1029/2018JA025712

Case, N. A., & Wild, J. A. (2012). A statistical comparison of solar wind propagation delays derived from multispacecraft techniques. *Journal of Geophysical Research*, *117*, A02101. https://doi.org/10.1029/2011JA016946

Chisham, G., Lester, M., Milan, S. E., Freeman, M. P., Bristow, W. A., Grocott, A., et al. (2007). A decade of the Super Dual Auroral Radar Network (SuperDARN): Scientific achievements, new techniques and future directions. *Surveys in Geophysics*, *28*(1), 33–109. https://doi.org/10.1007/s10712-007-9017-8

Cowley, S. W. H. (1981). Magnetospheric asymmetries associated with the y-component of the IMF. *Planetary and Space Science*, *29*(1), 79–96.

Cowley, S. W. H., & Lockwood, M. (1992). Excitation and decay of solar wind-driven flows in the magnetosphere-ionosphere system. *Annales Geophysicae*, *10*, 103–115.

Dungey, J. W. (1961). Interplanetary magnetic field and the auroral zones. *Physical Review Letters*, *6*(2), 47–48.

Escoubet, C. P., Schmidt, R., & Goldstein, M. L. (1997). Cluster—Science and mission overview. In C. P. Escoubet, C. T. Russell & R. Schmidt (Eds.), *The Cluster and Phoenix missions* (pp. 11–32). Dordrecht: Springer Netherlands.

Fear, R. C., & Milan, S. E. (2012). The IMF dependence of the local time of transpolar arcs: Implications for formation mechanism. *Journal of Geophysical Research*, *117*, A03213. https://doi.org/10.1029/2011JA017209

Georgescu, E., Puhl-Quinn, P., Vaith, H., Chutter, M., Quinn, J., Paschmann, G., & Torbert, R. (2010). EDI data products in the Cluster active archive. In Laakso, H., Taylor, M., & Escoubet, C. P. (Eds.), *The Cluster active archive* (pp. 83–95). Dordrecht: Springer Netherlands.

Grocott, A. (2017). Time-dependence of dawn-dusk asymmetries in the terrestrial ionospheric convection pattern. In S. Haaland, A. Runov, C. Forsyth (Eds.), *Dawn-dusk asymmetries in planetary plasma environments* (pp. 107–123). American Geophysical Union (AGU). https://doi.org/10.1002/9781119216346.ch9

Grocott, A., & Milan, S. E. (2014). The influence of IMF clock angle timescales on the morphology of ionospheric convection. *Journal of Geophysical Research: Space Physics*, *119*, 5861–5876. https://doi.org/10.1002/2014JA020136

Grocott, A., Yeoman, T. K., Milan, S. E., Amm, O., Frey, H. U., Juusola, L., et al. (2007). Multi-scale observations of magnetotail flux transport during IMF-northward non-substorm intervals. *Annales Geophysicae*, *25*(7), 1709–1720. https://doi.org/10.5194/angeo-25-1709-2007

Haaland, S. E., Paschmann, G., Förster, M., Quinn, J. M., Torbert, R. B., McIlwain, C. E., et al. (2007). High-latitude plasma convection from cluster EDI measurements: Method and IMF-dependence. *Annales Geophysicae*, *25*(1), 239–253. https://doi.org/10.5194/angeo-25-239-2007

Haaland, S., Paschmann, G., Förster, M., Quinn, J., Torbert, R., Vaith, H., et al. (2008). Plasma convection in the magnetotail lobes: Statistical results from Cluster EDI measurements. *Annales Geophysicae*, *26*(8), 2371–2382. https://doi.org/10.5194/angeo-26-2371-2008

Hanuise, C., Senior, C., Cerisier, J. C., Villain, J. P., Greenwald, R. A., Ruohoniemi, J. M., & Baker, K. B. (1993). Instantaneous mapping of high-latitude convection with coherent HF radars. *Journal of Geophysical Research*, *98*(A10), 17,387–17,400. https://doi.org/10.1029/93JA00813

Holappa, L., & Mursula, K. (2018). Explicit IMF by dependence in high-latitude geomagnetic activity. *Journal of Geophysical Research: Space Physics*, *123*, 4728–4740. https://doi.org/10.1029/2018JA025517

Hori, T., Maezawa, K., Saito, Y., & Mukai, T. (2000). Average profile of ion flow and convection electric field in the near-Earth plasma sheet. *Geophysical Research Letters*, *27*(11), 1623–1626. https://doi.org/10.1029/1999GL003737

Juusola, L., Østgaard, N., & Tanskanen, E. (2011). Statistics of plasma sheet convection. *Journal of Geophysical Research*, *116*, A08201. https://doi.org/10.1029/2011JA016479

Kabin, K., Rankin, R., Marchand, R., Gombosi, T. I., Clauer, C. R., Ridley, A. J., et al. (2003). Dynamic response of Earth's magnetosphere to $B_y$ reversals. *Journal of Geophysical Research*, *108*(A3), 1132. https://doi.org/10.1029/2002JA009480

Kessel, R. L., Chen, S.-H., Green, J. L., Fung, S. F., Boardsen, S. A., Tan, L. C., et al. (1996). Evidence of high-latitude reconnecting during northward IMF: Hawkeye observations. *Geophysical Research Letters*, *23*(5), 583–586. https://doi.org/10.1029/95GL03083

Khan, H., & Cowley, S. W. H. (1999). Observations of the response time of high-latitude ionospheric convection to variations in the interplanetary magnetic field using EISCAT and IMP-8 data. *Annales Geophysicae*, *17*(10), 1306–1335. https://doi.org/10.1007/s00585-999-1306-8

Khurana, K. K., Walker, R. J., & Ogino, T. (1996). Magnetospheric convection in the presence of interplanetary magnetic field $B_y$: A conceptual model and simulations. *Journal of Geophysical Research*, *101*(A3), 4907–4916. https://doi.org/10.1029/95JA03673

King, J. H., & Papitashvili, N. E. (2005). Solar wind spatial scales in and comparisons of hourly Wind and ACE plasma and magnetic field data. *Journal of Geophysical Research*, *110*, A02104. https://doi.org/10.1029/2004JA010649

Kissinger, J., McPherron, R. L., Hsu, T.-S., & Angelopoulos, V. (2012). Diversion of plasma due to high pressure in the inner magnetosphere during steady magnetospheric convection. *Journal of Geophysical Research*, *117*, A05206. https://doi.org/10.1029/2012JA017579

Liou, K., Sotirelis, T., & Mitchell, E. (2020). Control of the east-west component of the interplanetary magnetic field on the occurrence of magnetic substorms. *Geophysical Research Letters*, *47*, e2020GL087406. https://doi.org/10.1029/2020GL087406

Mailyan, B., Munteanu, C., & Haaland, S. (2008). What is the best method to calculate the solar wind propagation delay? *Annales Geophysicae*, *26*(8), 2383–2394. https://doi.org/10.5194/angeo-26-2383-2008

McFadden, J. P., Carlson, C. W., Larson, D., Ludlam, M., Abiad, R., Elliott, B., et al. (2008). The THEMIS ESA plasma instrument and in-flight calibration. *Space Science Reviews*, *141*(1), 277–302. https://doi.org10.1007/978-0-387-89820-9_13

Milan, S. E., Evans, T. A., & Hubert, B. (2010). Average auroral configuration parameterized by geomagnetic activity and solar wind conditions. *Annales Geophysicae*, *28*(4), 1003–1012. 12, https://doi.org10.5194/angeo-28-1003-2010

Milan, S. E., Gosling, J. S., & Hubert, B. (2012). Relationship between interplanetary parameters and the magnetopause reconnection rate quantified from observations of the expanding polar cap. *Journal of Geophysical Research*, *117*, A03226. https://doi.org/10.1029/2011JA017082

Milan, S. E., Grocott, A., & Hubert, B. (2010). A superposed epoch analysis of auroral evolution during substorms: Local time of onset region. *Journal of Geophysical Research*, *115*, A00I04. https://doi.org/10.1029/2010JA015663

Mukai, T., Machida, S., Saito, Y., Hirahara, M., Terasawa, M., Kaya, N., et al. (1994). The low energy particle (LEP) experiment onboard the GEOTAIL satellite. *Journal of Geomagnetism and Geoelectricity*, *46*, 669–692. https://doi.org/10.5636/jgg.46.669

Nishida, A. (1994). The Geotail mission. *Geophysical Research Letters*, *21*(25), 2871–2873. https://doi.org/10.1029/94GL01223

Ohma, A., Østgaard, N., Reistad, J. P., Tenfjord, P., Laundal, K. M., Moretto Jørgensen, T., et al. (2019). Observations of asymmetric lobe convection for weak and strong tail activity. *Journal of Geophysical Research: Space Physics*, *124*, 9999–10,017. https://doi.org/10.1029/2019JA026773

Ohma, A., Østgaard, N., Reistad, J. P., Tenfjord, P., Laundal, K. M., Snekvik, K., et al. (2018). Evolution of asymmetrically displaced footpoints during substorms. *Journal of Geophysical Research: Space Physics*, *123*, 10,030–10,063. https://doi.org/10.1029/2018JA025869

Østgaard, N., Mende, S. B., Frey, H. U., Immel, T. J., Frank, L. A., Sigwarth, J. B., & Stubbs, T. J. (2004). Interplanetary magnetic field control of the location of substorm onset and auroral features in the conjugate hemispheres. *Journal of Geophysical Research*, *109*, A07204. https://doi.org/10.1029/2003JA010370

Park, K. S., Ogino, T., & Walker, R. J. (2006). On the importance of antiparallel reconnection when the dipole tilt and IMF by are nonzero. *Journal of Geophysical Research*, *111*, A05202. https://doi.org/10.1029/2004JA010972

Paschmann, G., Melzner, F., Frenzel, R., Vaith, H., Parigger, P., Pagel, U., et al. (1997). The Electron Drift Instrument for Cluster. *Space Science Reviews*, *79*(1), 233–269. https://doi.org/10.1023/A:1004917512774

Petrukovich, A. A., & Lukin, A. S. (2018). Detailed regression model of plasma sheet by. *Journal of Geophysical Research: Space Physics*, *123*, 2872–2883. https://doi.org/10.1002/2017JA024993

Pettigrew, E. D., Shepherd, S. G., & Ruohoniemi, J. M. (2010). Climatological patterns of high-latitude convection in the Northern and Southern Hemispheres: Dipole tilt dependencies and interhemispheric comparisons. *Journal of Geophysical Research*, *115*, A07305. https://doi.org/10.1029/2009JA014956

Pitkänen, T., Hamrin, M., Karlsson, T., Nilsson, H., & Kullen, A. (2017). On IMF By-induced dawn-dusk asymmetries in earthward convective fast flows. In S. Haaland, A. Runov, C. Forsyth (Eds.), *Dawn-dusk asymmetries in planetary plasma environments* (pp. 95–106). American Geophysical Union (AGU). https://doi.org/10.1002/9781119216346.ch8

Pitkänen, T., Hamrin, M., Kullen, A., Maggiolo, R., Karlsson, T., Nilsson, H., & Norqvist, P. (2016). Response of magnetotail twisting to variations in IMF $B_y$: A THEMIS case study 1–2 January 2009. *Geophysical Research Letters*, *43*, 7822–7830. https://doi.org/10.1002/2016GL070068

Pitkänen, T., Hamrin, M., Norqvist, P., Karlsson, T., & Nilsson, H. (2013). IMF dependence of the azimuthal direction of earthward magnetotail fast flows. *Geophysical Research Letters*, *40*, 5598–5604. https://doi.org/10.1002/2013GL058136

Pitkänen, T., Kullen, A., Laundal, K. M., Tenfjord, P., Shi, Q. Q., Park, J.-S., et al. (2019). IMF $B_y$ influence on magnetospheric convection in Earth's magnetotail plasma sheet. *Geophysical Research Letters*, *46*, 11,698–11,708. https://doi.org/10.1029/2019GL084190

Reistad, J. P., Laundal, K. M., Ohma, A., Moretto, T., & Milan, S. E. (2020). An explicit IMF $B_y$ dependence on solar wind-magnetosphere coupling. *Geophysical Research Letters*, *47*, e2019GL086062. https://doi.org/10.1029/2019GL086062

Reistad, J. P., Østgaard, N., Laundal, K. M., Ohma, A., Snekvik, K., Tenfjord, P., et al. (2018). Observations of asymmetries in ionospheric return flow during different levels of geomagnetic activity. *Journal of Geophysical Research: Space Physics*, *123*, 4638–4651. https://doi.org/10.1029/2017JA025051

Reistad, J. P., Østgaard, N., Laundal, K. M., & Oksavik, K. (2013). On the non-conjugacy of nightside aurora and their generator mechanisms. *Journal of Geophysical Research: Space Physics*, *118*, 3394–3406. https://doi.org/10.1002/jgra.50300

Rème, H., Aoustin, C., Bosqued, J. M., Dandouras, I., Lavraud, B., Sauvaud, J. A., et al. (2001). First multispacecraft ion measurements in and near the Earth's magnetosphere with the identical Cluster ion spectrometry (CIS) experiment. *Annales Geophysicae*, *19*(10/12), 1303–1354.

Ruohoniemi, J. M., & Baker, K. B. (1998). Large-scale imaging of high-latitude convection with Super Dual Auroral Radar Network HF radar observations. *Journal of Geophysical Research*, *103*(A9), 20,797–20,811. https://doi.org/10.1029/98JA01288

Ruohoniemi, J. M., & Greenwald, R. A. (2005). Dependencies of high-latitude plasma convection: Consideration of interplanetary magnetic field, seasonal, and universal time factors in statistical patterns. *Journal of Geophysical Research*, *110*, A09204. https://doi.org/10.1029/2004JA010815

Russell, C. T. (1972). The configuration of the magnetosphere. In E. R. Dyer (Ed.), *Critical problems of magnetospheric physics* (pp. 1–16). Washington, DC: National Academy of Sciences.

Tenfjord, P., Østgaard, N., Haaland, S., Snekvik, K., Laundal, K. M., Reistad, J. P., et al. (2018). How the IMF $B_y$ induces a local $B_y$ component during northward IMF $B_z$ and characteristic timescales. *Journal of Geophysical Research: Space Physics*, *123*, 3333–3348. https://doi.org/10.1002/2018JA025186

Tenfjord, P., Østgaard, N., Snekvik, K., Laundal, K. M., Reistad, J. P., Haaland, S., & Milan, S. E. (2015). How the IMF $B_y$ induces a By component in the closed magnetosphere and how it leads to asymmetric currents and convection patterns in the two hemispheres. *Journal of Geophysical Research: Space Physics*, *120*, 9368–9384. https://doi.org/10.1002/2015JA021579

Tenfjord, P., Østgaard, N., Strangeway, R., Haaland, S., Snekvik, K., Laundal, K. M., et al. (2017). Magnetospheric response and reconfiguration times following IMF $B_y$ reversals. *Journal of Geophysical Research: Space Physics*, *122*, 417–431. https://doi.org/10.1002/2016JA023018

Thomas, E. G., & Shepherd, S. G. (2018). Statistical patterns of ionospheric convection derived from mid-latitude, high-latitude, and polar SuperDARN HF radar observations. *Journal of Geophysical Research: Space Physics*, *123*, 3196–3216. https://doi.org/10.1002/2018JA025280

Vokhmyanin, M. V., Stepanov, N. A., & Sergeev, V. A. (2019). On the evaluation of data quality in the OMNI interplanetary magnetic field database. *Space Weather*, *17*(3), 476–486. https://doi.org/10.1029/2018SW002113